ACS OMEGA

Open Access

This article is licensed under CC-BY-NC-ND 4.0

http://pubs.acs.org/journal/acsodf

Article

Evolution Path of Precursor-Induced High-Temperature Lithiation Reaction during the Synthesis of Lithium-Rich Cathode Materials

Chen Wu, Jiuqing Ban, Ting Chen, Jie Wang, Yangdong He, and Zhen-guo Wu*

Cite This: *ACS Omega* 2024, 9, 15191−15201

Read Online

ACCESS | Metrics & More | Article Recommendations | Supporting Information

ABSTRACT: High-temperature lithiation is one of the crucial steps for the synthesis of Li- and Mn-rich layered metal oxide (LMLO) cathodes. A profound insight of the micromorphology and crystal structure evolution during calcination helps to realize the finely controlled preparation of final cathodes, finally achieving a desired electrochemical performance. In this work, two typical precursors (hydroxide and oxalate) were selected to prepare LMLO. It is found that the influence of the lithium source on reaction pathways is determined by the properties of precursors. In the case of hydroxide as a precursor, whatever lithium sources it is, the flake morphology of LMLO is inherited from hydroxide precursors. This is because the crystal structure of cathode products has a high similarity with its precursor in terms of the oxygen array arrangement, and the topological transformation occurs from hydroxide ($P\bar{3}ml$) to LMLOs ($C/2m$ and $R\bar{3}m$). Thus, the morphology and microstructure of LMLO cathodes could be well controlled only by tuning the properties of hydroxide precursors. Conversely, the decomposition of a lithium source has a great influence on the intermediate transformation when oxalate is used as the precursor. This is because a large amount of CO_2 is released from the oxalate precursor after the decomposition reaction, resulting in drastic structural changes. At this time, the diffusion ability of the lithium source leads to the competition between the spinel phase and layered phase. Based on this point, the formation of a spinel intermediate phase can be reduced by accelerating the decomposition of the lithium source, contributing to the generation of a highly pure layered phase, thus exhibiting higher electrochemical performance. These insights provide an exciting cue to the rational selection and design of raw materials and lithium sources for the controlled synthesis of LMLO cathodes.

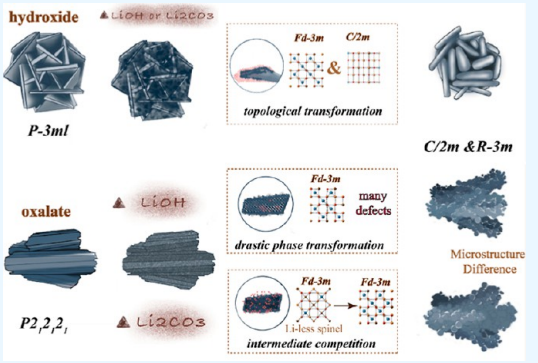

INTRODUCTION

To meet the requirements of electric vehicles and large-scale energy storage systems, the development of a higher energy density lithium-ion battery has become very urgent.[1−5] With a high theoretical capacity and low cost, Li- and Mn-rich layered transition metal oxides (LMLO), which are a promising class of cathode materials, have drawn intensive attention in recent years.[6−10] The coprecipitation route followed by a solid-state reaction has been widely studied as a mainstream fabrication method to achieve high-performance lithium-ion cathode materials.[11−15] Although the solid-state reaction is simple in operation, the synthesis route undergoes complex chemical reactions, such as decomposition process, solid phase diffusion, nuclear reaction, and crystal growth, which is unclear and should be studied from the structure of the original materials.[16−19]

In the synthesis of lithium-ion cathode materials, solid-state reactions typically take place through multiple intermediate reaction steps.[20,21] The produced nonequilibrium intermediates may act as templates for subsequent phase transformation or remain as impurities in final compounds.[17,22] It is reported that $LiCoO_2$ is synthesized by metastable spinel intermediates (Co_3O_4 and $Li_2Co_2O_4$; $Fd\bar{3}m$). While $LiNiO_2$ and its solid solution ($LiNi_{0.8}Co_{0.2}O_2$) are synthesized by rock-salts (Ni,Co)O and then disordered rock-salts [$Li_x(Ni,Co)_{2-x}O_2$; $Fm\bar{3}m$], finally forming $Li_x(Ni,Co)O_2$ with undesired high Li/Ni mixing.[23] In addition, the transition temperature of the layered structure during the synthesis of $LiNi_{0.6}Co_{0.2}Mn_{0.2}O_2$ using $Ni_{0.6}Co_{0.2}Mn_{0.2}(OH)_2$ is lower than that using $Ni_{0.6}Co_{0.2}Mn_{0.2}CO_3$.[24] Moreover, the lithium exceeding stoichiometric ratio causes the residual lithium on the surface and occupancy of Li/Ni mixed arrangement,[25] while the lack of lithium content generates impurity phase during the preparation of $LiTMO_2$ (TM = Ni, Co, Mn, Al. . .).[26] The structural and compositional dependence of manganese-rich lithium insertion compounds on the lithium provided during synthesis was investigated.[27] The selection of different lithium sources could control the reaction pathways of $Ni_{0.25}Mn_{0.75}CO_3$ in low temperature and then prepare the Li-rich cathode with high-

Received: November 30, 2023
Revised: February 7, 2024
Accepted: February 9, 2024
Published: March 18, 2024

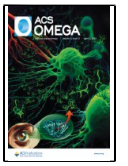

© 2024 The Authors. Published by American Chemical Society

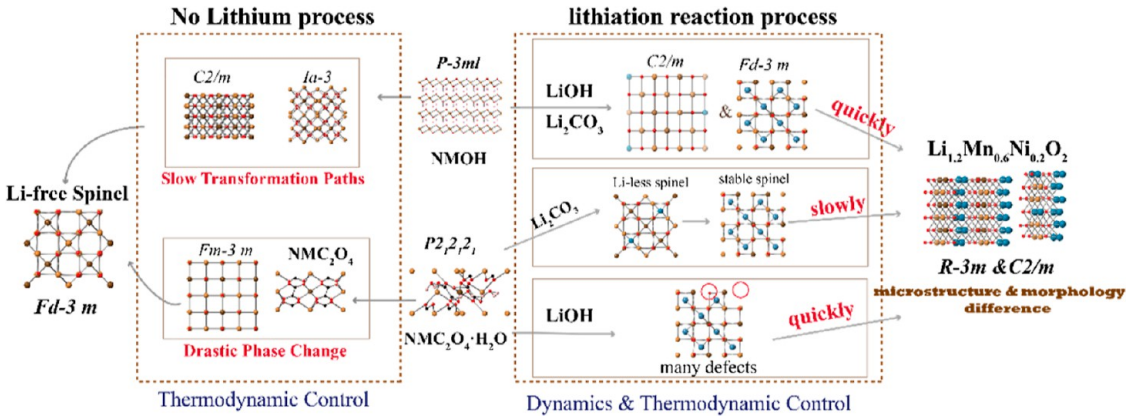

Figure 1. Schematic illustration for the phase transition during the high-temperature reaction between different precursors and without/with lithium source (NMOH means hydroxide and $NMC_2O_4.H_2O$ means oxalate.).

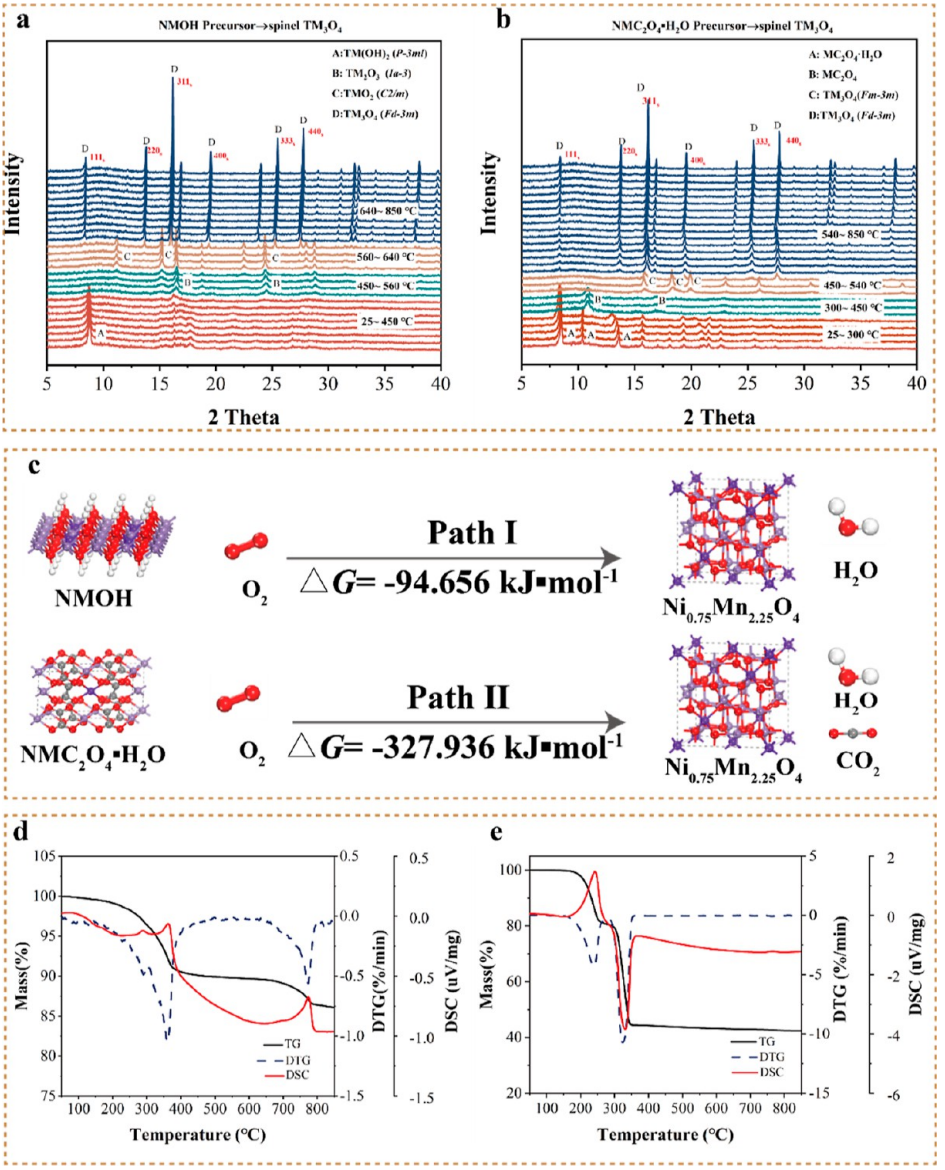

Figure 2. In situ high-temperature synchrotron radiation diffraction patterns of the precursor without a lithium source, (a) NMOH, (b) $NMC_2O_4\cdot H_2O$; (c) the Gibbs free energy change from precursors to spinel structure; and TG/DSC curves of (d) NMOH and (e) $NMC_2O_4\cdot H_2O$.

rate performance.[28] A lot of works show that the type of precursors and lithium source have an effect on the intermediate phase structure evolution, affecting the microstructure, particle size, and morphology of the final product, finally changing the

https://doi.org/10.1021/acsomega.3c09567
ACS Omega 2024, 9, 15191−15201

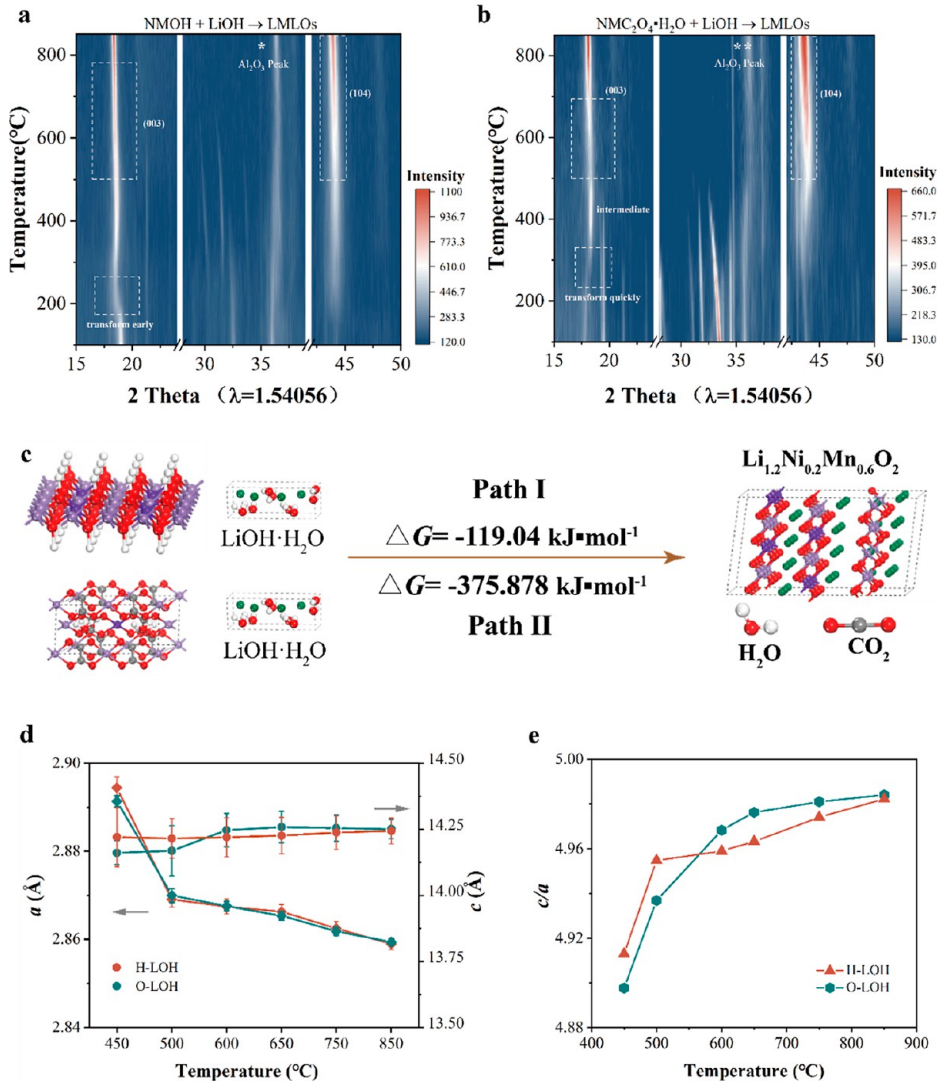

Figure 3. In situ high-temperature radiation diffraction patterns of the mixture system: (a) H-LOH and (b) O-LOH; (c) the Gibbs free energy change from raw materials to layered $Li_{1.2}Mn_{0.6}Ni_{0.2}O_2$ structure; and the lattice parameters of the specimens as a function of heating temperature starting from mixture system quenching at different temperatures (the data of XRD were refined on a hexagonal α-$NaFePO_2$ structure with the $R\bar{3}m$ space group), (d) parameters of c and a, and (e) the ratio value of c/a.

electrochemical performance.[29−34] However, due to the complexity of the calcination process, there is still a lack of systematic research on the influence of the types of lithium sources on the evolution path selection of different precursors.

In this work, two typical precursors [hydroxide (NMOH) and oxalate ($NMC_2O_4{\cdot}H_2O$), both NM = Ni and Mn] and two regular lithium sources (LiOH and Li_2CO_3) were selected to prepare LMLO. In situ high-temperature synchrotron radiation diffraction (HTSRD) and in situ high-temperature X-ray radiation diffraction (HTXRD) were utilized to investigate the structure evolution without and with lithium source. As shown in Figure 1, both the different precursors convert into lithium-free spinel TM_3O_4 through different transformation pathways. For NMOH precursors, the slow topological transition occurs spinel phase is formed at high temperature (>640 °C). The structure evolution and morphology of LMLOs prepared from NMOH are inherited and not affected by the types of lithium sources. Both them change from layered *P-3 mL* to spinel/rock-salt ($Fd\bar{3}m/Fm\bar{3}m$) and quickly convert into disorder/order layered phase ($C/2m$ and $R\text{-}\bar{3}m$). The prepared cathodes exhibit a similar electrochemical performance. In contrast, the $NMC_2O_4{\cdot}H_2O$ precursors undergo a rapid phase transition and form a spinel phase at a lower temperature (<450 °C) during calcination without lithium. While after lithium source adding, the reaction converts into layered structure quicky when mixing with LiOH. However, when mixing with Li_2CO_3, it converts into the stable lithium-poor spinel intermediate ($Fd\bar{3}m$) in the early stage (below 500 °C). This is because a large amount of CO_2 released after $NMC_2O_4{\cdot}H_2O$ decomposition leads to the collapse of the original structure and the formation of a poor crystal or amorphous structure. The ΔG values from original materials to the spinel structure and to layered $Li_{1.2}Mn_{0.6}Ni_{0.2}O_2$ product are closed, resulting in the competition between the spinel and layered structure in the reaction process. This process makes a great difference between the microstructure and morphology of LMLO materials, thereby affecting the electrochemical performance. These insights may provide a reference for the controlled synthesis of advanced electrode materials with a rational selection and design of raw materials.

https://doi.org/10.1021/acsomega.3c09567
ACS Omega 2024, 9, 15191−15201

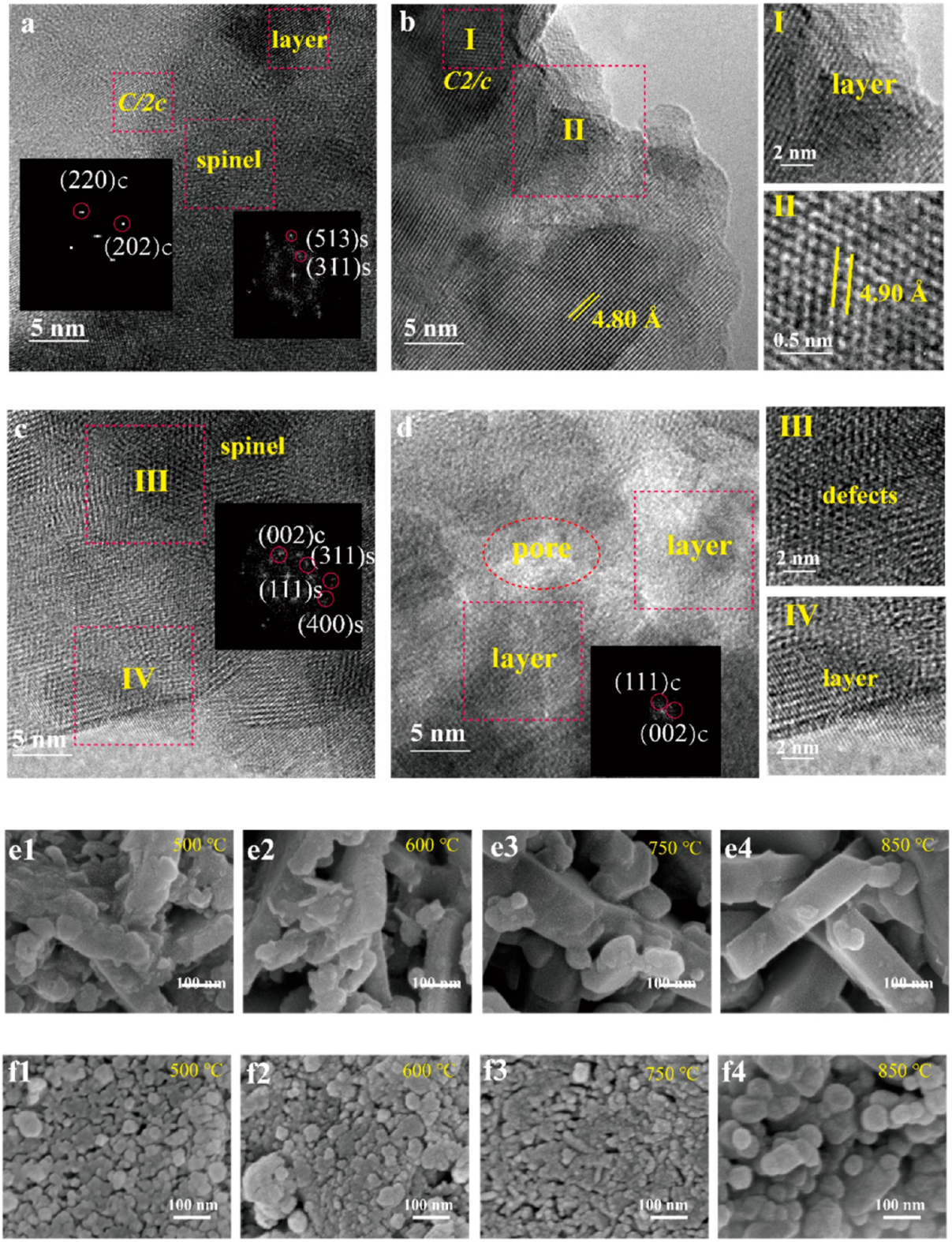

Figure 4. HRTEM images of the mixture system quenching at 450 and 500 °C. (a) H-LOH at 450 °C, (b) H-LOH at 500 °C, (c) O-LOH at 450 °C, and (d) O-LOH at 500 °C; SEM images of mixture system quenching at 500, 600, 750, and 850 °C (from left to right), respectively. (e) H-LOH and (f) O-LOH.

DISCUSSION AND RESULT

Both NMOH and $NMC_2O_4{\cdot}H_2O$ with the same Ni/Mn ratio of 1:3 were prepared by coprecipitation (Table S1 and Figure S1).[35] First, in situ high-temperature synchrotron radiation diffraction was utilized to trace the structural evolution of different precursors without a lithium source.[36] As shown in Figure 2a-b, although all precursors are converted into single cubic spinel TM_3O_4 ($Fd\bar{3}m$), these go through different pathways when heating up to 850 °C. The ΔG from different

https://doi.org/10.1021/acsomega.3c09567
ACS Omega 2024, 9, 15191−15201

precursors to the final spinel TM_3O_4 structure are shown in Figure 2c, ΔG is −327.936 kJ·mol^{-1} in the oxalate system and −94.656 kJ·mol^{-1} in the hydroxide system. It is indicated that the reaction of the $NMC_2O_4{\cdot}H_2O$ is thermodynamically more favorable to occur. Combined with the thermogravimetric and differential scanning calorimetric analysis (TG/DSC) shown in Figure 2d-e, NMOH decomposes from the initial hexagonal structure *P-3 mL* to *Ia-3*above 400 °C, to *C2/m* at ∼540 °C, and finally deoxidized above 650 °C to convert into $Fd\bar{3}m$. $NMC_2O_4{\cdot}H_2O$ is heated to lose crystal water at 200−300 °C, and CO_2 is out to convert into $Fm\bar{3}m$ about 300−400 °C and forms a spinel at 540 °C.[37] Moreover, the DSC drops sharply when $NMC_2O_4{\cdot}H_2O$ decomposes. Both the results of X-ray diffraction (XRD) and TG/DSC show that the transformation process from the precursor of NMOH to the spinel structure is more difficult than that of $NMC_2O_4{\cdot}H_2O$. Moreover, the morphology evolution is shown as Figure S2. Although the NMOH reaction is more difficult to carry out, the primary particle morphology of the final product is similar, which is caused by the morphology dominated by the spinel crystal structure after long-term high-temperature sintering. This indicates that the morphology of the final product is not only related to the morphology of the precursor but also to the changes in the crystal phase.

In order to investigate the influence of precursors on the high-temperature lithiation process, LMLO was prepared by mixing NMOH and $NMC_2O_4{\cdot}H_2O$ with LiOH (marked as H-LOH and O-LOH, respectively). According to in situ high-temperature XRD, the lithiation reaction mechanism can be divided into three stages (Figure S3). In H-LOH, as illustrated in Figure 3a, the decomposition process of the NMOH and LiOH, including the dehydration decomposition process of the LiOH and NMOH is below 150 °C. While above 200 °C, a set of new reflections of 18.5° and 43.9° that can be indexed to the $(003)_L$ and $(104)_L$ peak associated with lithium-poor transition metal oxides $[Mn_{0.75}Ni_{0.25}(OH_{1-x}Li_y)_2]$ begin to appear[37] [these two peaks are marked as $(003)_L$ and $(104)_L$ in the subsequent process for comparison], which may be assigned to the $Fd\bar{3}m$ or *I-3a* space group.[38] At 500−625 °C, the $(003)_L$ peak changes little but the $(104)_L$ peak grows rapidly, indicates the structure transforms to layered $Li_xMn_{0.75}Ni_{0.25}O_2$ ($0 < x < 0.5$) structure, but with serious Li/TM mixing. Both $(003)_L$ and $(104)_L$ peaks grow up quickly and become narrower when heating up to 625 °C, and the splitting of the two reflections of $006_{T2}/012_{T2}$ (2θ = 38°) and $018_{T2}/110_{T2}$ (2θ = 64.5°) appears at same time. It indicates that the crystallinity of the layered structure increases and the Li/TM arrangement becomes orderly.[39] In O-LOH, as illustrated in Figure 3b, the XRD peaks change dramatically around 200 °C. This is because $NMC_2O_4{\cdot}H_2O$ loses the crystal water and reacts with LiOH to form $Mn_{0.75}Ni_{0.25}C_2O_4$ and $Li_2C_2O_4$. As the temperature continue to increase, unreacted $Mn_{0.75}Ni_{0.25}C_2O_4$ decomposes and forms to lithium-containing transition metal oxides $Li_xMn_{0.75}Ni_{0.25}O_y$ ($0 < x < 0.5$), which is assigned to the spinel/layer phase. The peak of $(003)_L$ (Figure S4) in O-LOH is weakened and widened significantly at 500 °C, indicating that a drastic phase transition may have occurred from spinel to the layered structure. With the increase of the temperature, the impurity peak decreases and the peak width narrows gradually. Peak splitting begins to occur above 700 °C. The ΔG from different precursors to layered $Li_{1.2}Mn_{0.6}Ni_{0.2}O_2$ structure varies greatly, as shown in Figure 3c. The results indicate that the reaction is theoretically more likely to occur in O-LOH. However, the contour plots of in situ XRD patterns of the lithiation process (Figure S3) shows that the similar layered structure can also be quickly formed in H-LOH below 500 °C. The above results indicate that after embedding into Li/O, NMOH and $NMC_2O_4{\cdot}H_2O$ undergo different intermediate structures to transform into the final product.[40]

The thermogravimetry-mass spectra (TG-MS) are shown in Figure S5. There is no significant weight loss above 500 °C, and no CO_2 and H_2O are detected, indicating that the sample decomposition was mainly within 500 °C. Combined with the actual lithiation reaction, these mixture systems including H-LOH and O-LOH were pretreated at 500 °C for 5 h and heated at 850 °C for 12 h in an air atmosphere with a heating rate of 5 °C min^{-1} to further investigate the difference of the evolution process. Both of them were quenched at 350, 450, 500, 600, 650, 750, and 850 °C to observe the structure and morphology evolution. The XRD results as illustrated in Figure S6 clearly show that structures of NMOH and $NMC_2O_4{\cdot}H_2O$ have been converted into a new lithium-containing phase at 350 and 450 °C. Apparently, after quenching at 500 °C for 5 h, the characteristic peaks of LiOH and $Li_2C_2O_4$ disappear, and both the mixture systems convert into a layered structure, as shown in Figure S7. The Rietveld refinement method was applied to analyze XRD patterns by Fullprof software. The results are shown in Figure 3d. In O-LOH, the parameters *c* and *a* change sharply after 500 °C, indicating that the significant phase transition occurs. The ratio value of *c/a* (from Figure 3e) demonstrates that the structure might be from spinel/disorder to layer.[21,41] With temperature increasing, parameter *a* decreases, but parameter *c* increases. The ratio value of *c/a* in O-LOH is lower than that of H-LOH at 500 °C, but larger than that of H-LOH above 600 °C, which means O-LOH is more likely to form ordered layered structures than H-LOH above 600 °C.[13]

The HRTEM images of H-LOH quenching at 450 and 500 °C are observed as shown in Figure 4a-b, and both of them have good crystallinity. Through the corresponding fast Fourier transform (FFT) patterns and lattice spacing, it can be identified that there are a large number of layered phases *(C/2m)* and a few spinel phases ($Fd\bar{3}m$) at 450 °C. Most of them are fitted with layered at 500 °C. The HRTEM images of O-LOH quenching at 450 and 500 °C were observed, as shown in Figure 4c-d. The spinel structure can be observed at 450 °C in O-LOH with many defects. Both the layered structures can be easily observed on the surface at 450 °C, which means that the lithium ions are inserted from the surface to the inside. Correspondingly, most of the structure becomes a layered structure in O-LOH at 500 °C. The Raman spectra of H-LOH and O-LOH quenching at 500 °C are illustrated in Figure S8. There are obvious Li_2MnO_3 characteristic peaks in H-LOH but not in O-LOH. This also indicates that the H-LOH is beneficial to the formation of the *C/2m* phase in the low temperature stage. The morphological changes of the particles during the lithiation reaction process were detected by scanning electron microscopy (SEM). The morphology evolutions of H-LOH are shown in Figure 4e. There is a layer of materials on the surface of H-LOH, which may be unreacted LiOH at low temperature (<500 °C). Continue heating up, many small particles are formed. In the high temperature stage (above 750 °C), some small primary particles disappear, and the crystals grow up, then convert into thick, densely packed flake product. Apparently, the structure from NMOH (*P-3 mL*) to LMLOs (*C/2m* and $R\bar{3}m$) materials go through topological transformation with similar oxygen stacking. This is because the *P-3ml* and $R\bar{3}m/C/2m$ structures belong to the trigonal and

https://doi.org/10.1021/acsomega.3c09567
ACS Omega 2024, 9, 15191−15201

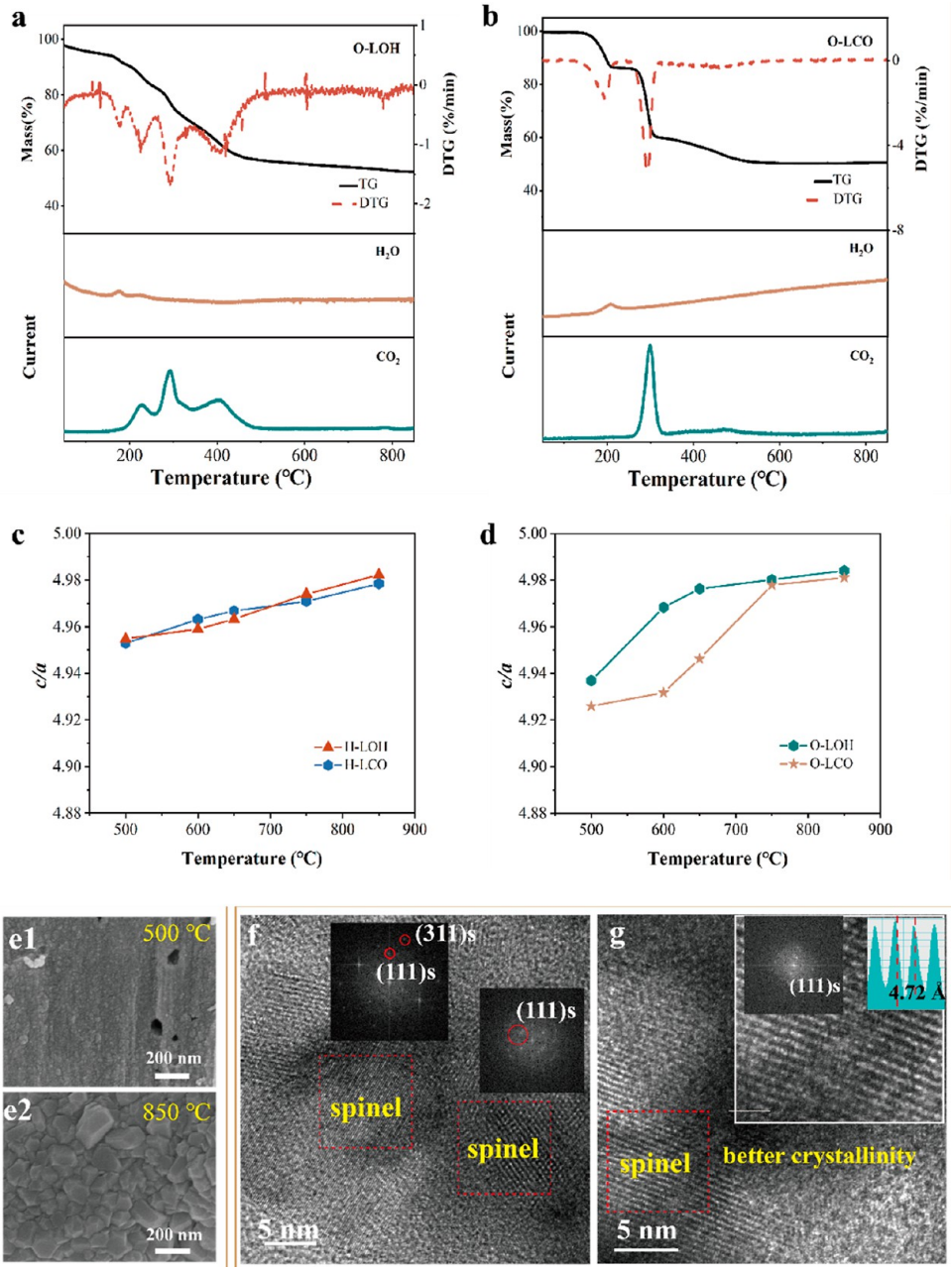

Figure 5. TG-MS spectra of oxalate mixing with different lithium sources, H_2O and CO_2 during high temperature calcination were detected by mass spectrometry (a) O-LOH, (b) O-LCO; the lattice parameters of the specimens as a function of heating temperature starting from the different precursors (NMOH and $NMC_2O_4{\cdot}H_2O$) mixing with LiOH and Li_2CO_3 quenching at different temperatures (the data of XRD were refined on a hexagonal α-$NaFePO_2$ structure with the $R\bar{3}m$ space group): (c) NMOH and (d) $NMC_2O_4{\cdot}H_2O$; (e) SEM images of O-LCO quenching at 500 and 850 °C; and HRTEM images of O-LCO quenching at (f) 450 and (g) 500 °C.

hexagonal crystal systems, respectively, and their oxygen atoms are arranged in a hexagonal tightly packed arrangement. The morphology evolutions of O-LOH are shown in Figure 4f. The O-LOH becomes pulverized and coarse after CO_2 escapes at low temperature (<500 °C). With temperature increasing, the particles regrow up, and the primary particles of final materials are evenly distributed with a polygonal shape. Obviously, the morphology of O-LOH has undergone significant changes from the precursor to the finished product, due to the loss of a large amount of CO_2 and H_2O in the structure, resulting in a drastic phase transition. In summary, the shapes of NMOH and LMLOs are packed flake with morphological inheritance, but the drastic phase transformation occurs in O-LOH and the primary particles change from the original flake shapes to polyhedral particles. It shows that the morphology evolution process is closely related to the reaction pathways.

To further judge the influence of the lithium source on the evolution process during high-temperature lithiation reactions, LMLO was prepared by mixing NMOH and $NMC_2O_4{\cdot}H_2O$ with Li_2CO_3, respectively (marked as H-LCO and O-LCO, respectively). The TG analyzing (as Figure S9) shows that the melting point of LiOH is about 450 °C and that of Li_2CO_3 is about 720 °C. The TG-MS of H-LCO is shown in Figure S10. The decomposition temperature of Li_2CO_3 in the H-LCO system is around 350 °C, indicating that transition metals promote the decomposition of Li_2CO_3. TG-MS spectra of O-

https://doi.org/10.1021/acsomega.3c09567
ACS Omega 2024, 9, 15191−15201

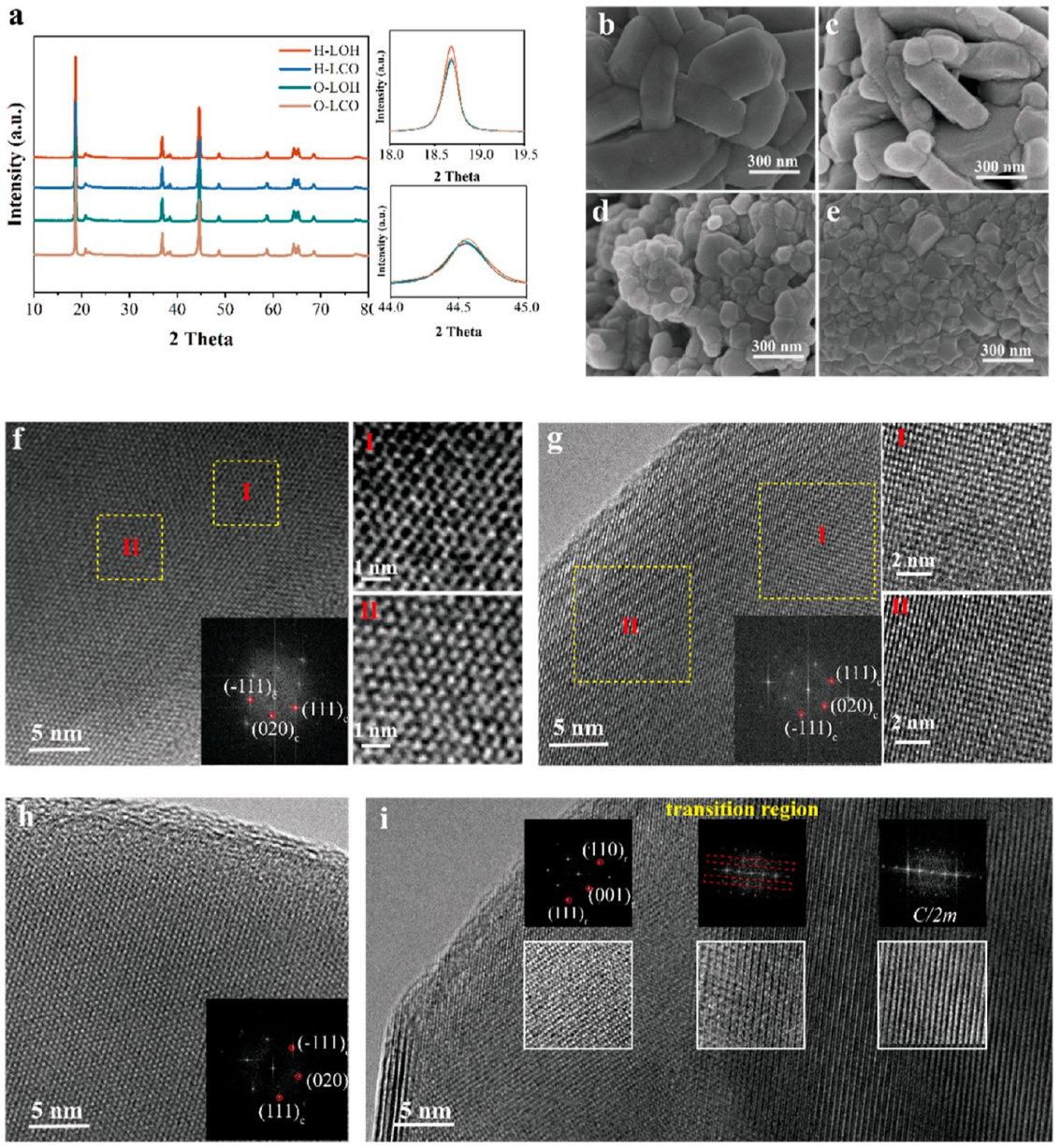

Figure 6. XRD patterns of LMLO through different raw materials (a); SEM images of LMLOs from (b) H-LOH, (c) H-LCO, (d) O−LOH, and (e) O−LCO; and HRTEM images of LMLO from (f) H-LOH, (g) H-LCO, (h) O−LOH, and (i) O−LCO.

LOH and O-LCO are shown in Figure 5a-b. Apparently, there are three CO_2 mass-spectra detection peaks in O-LOH, corresponding to the reaction of LiOH and $NMC_2O_4{\cdot}H_2O$, the decomposition of the unreacted NMC_2O_4 and the decomposition of $Li_2C_2O_4$. While the decomposition of $NMC_2O_4{\cdot}H_2O$ in O-LCO is the same as the lithium-free system (as illustrated in Figure 2d). The Li_2CO_3 starts to decompose and the lithium ion intercalates into the inherent structure after $NMC_2O_4{\cdot}H_2O$ decomposes. This indicates that in the O-LOH and O-LCO systems, the decomposition temperature of Li_2CO_3 is still higher than that of LiOH. From the XRD peaks of Figure S6, both the characteristic peaks change compared to no-lithium decomposition pathways. The intensity of peaks using different lithium sources also changes. While the crystallinity of H-LOH is better than that of H-LCO at 350 and 450 °C, the crystallinity of O-LCO is better than that of O-LOH. This is because when NMOH is used, topological transformation occurs due to the lithium ions' insertion. The rapid decomposition of the LiOH is conducive to the diffusion of Li^+ in the bulk phase. When $NMC_2O_4{\cdot}H_2O$ is used, the slow decomposition of Li_2CO_3 in O-LCO causes faster low-lithium spinel phase transition and growth. As illustrated in Figure S11, the ΔG from $NMC_2O_4{\cdot}H_2O$ to lithium-free spinel structure and to layered $Li_{1.2}Ni_{0.2}Mn_{0.6}O_2$ with $LiOH/Li_2CO_3$ are −327.936, −375.84, and −283.296 $kJ{\cdot}mol^{-1}$, respectively. This indicates that the reaction without lithium is more likely to occur than that of O-LCO. Further compare the results of Rietveld refinement of XRD spectrum, as shown in Figure 5c-d and Figure S12. In the NMOH system, there is not much difference in the c/a values between H-LOH and H-LCO at the same temperature. However, in the $NMC_2O_4{\cdot}H_2O$ system, there is a significant difference between O-LOH and O-LCO, which only approaches at 750 °C. It demonstrates that the temperature of phase transformation from the spinel to ordered layer structure in O-LCO is much higher than that of O-LOH. HRTEM images of O-LCO quenching at 450 and 500 °C are shown in Figure 5f-g.

https://doi.org/10.1021/acsomega.3c09567
ACS Omega 2024, 9, 15191−15201

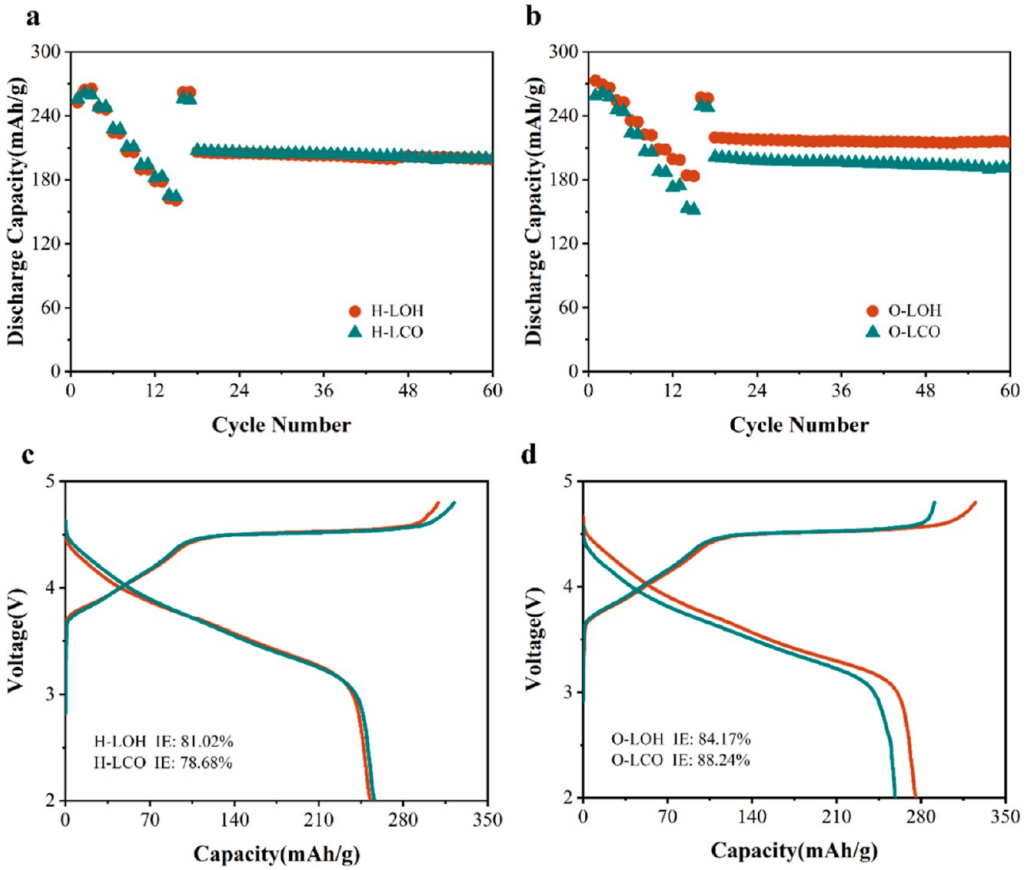

Figure 7. Comprehensive electrochemical performance of the LMLO between 2.0 and 4.8 V at 25 °C: (a) LMLOs from NMOH and (b) LMLO from $NMC_2O_4{\cdot}H_2O$; the initial charge−discharge voltage profiles: (c) LMLO from NMOH and (d) LMLO from $NMC_2O_4{\cdot}H_2O$.

This indicates that O-LCO forms a spinel phase with good crystallinity at 450 °C, which increases the difficulty of structural transition to a layered structure. The morphology evolutions during the lithiation reaction in H-LCO are shown in Figure S13 and Figure 5e. It is obvious that the surface of H-LCO is rougher than that of H-LOH at a high temperature but with similar flake primary particles. Therefore, we reasonably guess that the transformation pathway is one of the key factors affecting the morphology of the final product. The topological structure transition occurs from NMOH to LMLOs, resulting in inherited morphology. Furthermore, the morphological evolution of the $NMC_2O_4{\cdot}H_2O$ system was compared. The surface of O-LOH is denser than that of O-LCO, and the shapes of primary particles are different. The specific surface area was calculated by the Brunauer−Emmett−Teller (BET) method to compare the morphology difference with different lithium sources. As shown in Table S6, the specific surface area of NMOH is 15.594 $m^2{\cdot}g^{-1}$. Quenching the mixtures at 500 and 650 °C, the specific surface areas of H-LOH are 11.411 and 6.374 $m^2{\cdot}g^{-1}$, and for H-LCO, are 6.919 and 5.650 $m^2{\cdot}g^{-1}$. For oxalate, the specific surface area of the precursor is 10.181 $m^2{\cdot}g^{-1}$, 38.369 and 25.347 $m^2{\cdot}g^{-1}$ for O-LOH, and 23.684 and 20.141 $m^2{\cdot}g^{-1}$ for O-LCO, respectively. The obvious difference of shapes and specific surface area of O-LOH and O-LCO reaction process also indicates that the transformation pathway is the key factor of morphology evolution. During the decomposition process of $NMC_2O_4{\cdot}H_2O$, a large amount of CO_2 and H_2O are released, leading to a drastic phase transition of the structure. At this time, the speed at which lithium sources participate in the reaction leads to the generation of different types of morphologies.

The LMLO was sintered up under the same condition to identify the influence of raw materials and influence on the electrochemical performance. Structure information on all final products was studied by XRD, as shown in Figure 6a. Rietveld refinement results for diffraction patterns show that both structures combine the rhombohedral symmetry with space group *R*-$\bar{3}$*m* and monoclinic symmetry of the Li/Mn ordering superlattice within 20−25°. However, the intensity of the $(003)_L$/ $(104)_L$ peak is different, indicating the difference in the atom arrangement of Li/TM. The SEM images of final products are shown in Figure 6b-e, and these show that the lithium source affects the sizes, shapes, and stacking of primary particles. The primary particles of LMLO using NMOH are flakey, which is inherited by the NMOH precursor. Meanwhile, the primary particles when using $NMC_2O_4{\cdot}H_2O$ are polyhedral in shape and affected by the types of lithium source. Comparing the microstructures of H-LOH and H-LCO through HRTEM as shown in Figure 6f-g, all structures with fine crystallinity are fitted with a uniform *C2/m* and *R*-$\bar{3}$*m* structure. However, in the microstructure of O-LOH as shown in Figure 6h, the *C2/m* and *R*-$\bar{3}$*m* structures cannot be clearly distinguished. Figure 6i presents the TEM image of O-LCO and its corresponding FFT patterns. There is an obvious nonuniform phase distribution on the same primary particle, which is indexed as *Fm*-$\bar{3}$*m*, transition region, and *C2/m* structures, respectively. Therefore, different raw materials will cause differences in the morphology and the microstructure of final products.

Figure 7a-c and Figure S14 show the rate and cycling performance which were tested in different rates (0.1 C, 0.2 C, 0.5 C, 1 C, 2 C, 3 C, and 5 C, defined as 1 C = 250 mA h g^{-1}) for

https://doi.org/10.1021/acsomega.3c09567
ACS Omega 2024, 9, 15191−15201

two cycles at each step and continues cycling at 1 C between 2.0 and 4.8 V at room temperature. Both LMLO from H-LOH and H-LCO exhibit the similar electrochemical performance, indicating that the influence of the lithium source in NMOH system is relatively small. The LMLO from O-LOH with smaller and looser primary particles display the best rate capacities, which are 270.2, 256.3, 239.5, 226.2, 214.1, 203.5, and 189.5 mA h g^{-1}, respectively. Whereas LMLO from O-LCO has 261.4 mA h g^{-1} at 0.1C, but 153.1 mA h g^{-1} at 5C. This indicates that the rate performance of O-LCO is far inferior to that of O-LOH. After 50 cycles, the discharge capacity of LMLO from O-LOH is much higher than that of other electrodes, but O-LCO is the worst (such as LMLO from H-LOH is 198.8, H-LCO is 199.9, O-LOH is 217.4, and O-LCO is 193.5 mA h g^{-1}). The first charge/discharge curves are present in Figure 7c-d. The curves within the charging range of 4.45 V almost overlap, and there is a difference above 4.45 V, indicating that the Ni^{2+}/Ni^{4+} redox couple during the charging process has similar electrochemical behaviors but the O^{2-}/O^{x-} redox is different. The O^{2-}/O^{x-} redox is closely related to the local electronic structure which might depend on the uniform recombination of Li_2MnO_3 and $LiTMO_2$. Apparently, the LMLO from $NMC_2O_4{\cdot}H_2O$ exhibits higher initial capacity retention than that from NMOH. This is because its primary particles are smaller, which is more conducive to the full progress of electrochemical reactions. The increase in capacity of LMLO synthesized by NMOH in the first three cycles further confirms this viewpoint. Based on the previous text, it can be seen that the synthesis of LMLO through NMOH mainly relies on the topological changes between layered structures. The influence of the type of lithium source on the synthesis process and the microstructure of the final product is relatively small, and its electrochemical performance is also minimally affected by the lithium source. However, the synthesis of LMLO through $NMC_2O_4{\cdot}H_2O$ mixing with Li_2CO_3, the intermediate reaction pathway undergoes a severe phase transition from lithium-free spinel to layered phases, which is relatively more difficult to achieve and may be difficult to achieve complete transformation at high temperatures. Therefore, LMLO from O-LOH exhibits the best electrochemical performance, but worst in O-LCO. The synthesis of LMLO from NMOH can better control the morphology and microstructure, thereby obtains the stable electrochemical performance.

In order to further verify that the electrochemical performance of NMOH is not significantly affected by the lithium source, different sintering temperatures were selected for investigation, including 800, 850, and 900 °C, and their performance is shown in Figure S15. It can be seen that due to the existence of the optimal sintering temperature, different sintering temperatures will have a certain impact on the capacity and rate performance of electrochemical performance. However, at the same temperature, the synthesized LMLO does not show significant differences due to the type of lithium source.

CONCLUSIONS

In summary, a systematic study on the structure and morphologies evolution of different precursors with/without lithium hydroxide was performed. In situ high-temperature XRD and Gibbs free energy(ΔG) calculation were used to fulfill detailed experimental and theoretical exploration of the high-temperature lithiation process. All results indicate that when the raw material is sintered in the absence of lithium, NMOH undergoes a series of slow phase transitions and can only complete the transformation of the spinel phase structure at higher temperatures, while $NMC_2O_4{\cdot}H_2O$ undergoes a drastic phase transition after decomposition and transforms into a lithium free spinel structure at lower temperatures. When LMLO is synthesized by NMOH, the reaction pathway undergoes a topological phase transition from hydroxide ($P\bar{3}m1$) to LMLO ($C/2m$ and $R\bar{3}m$). Both of them are layered structures, and their evolution process has a certain degree of inheritance. The microstructure, morphology, and electrochemical performance of the final product are almost unaffected by the type of lithium source. When LMLO is synthesized by $NMC_2O_4{\cdot}H_2O$, the diffusion ability of lithium sources leads to the competition between spinel and layered phases. LiOH can react with its precursor at room temperature, rapidly evolving into a disordered rock salt structure and transforming into a disordered layered structure, ultimately becoming a highly crystalline ordered layered structure at high temperatures. However, Li_2CO_3 cannot react with the precursor at room temperature and needs to be decomposed and reacted with the precursor at 300−550 °C. The precursor undergoes a severe phase transition after decomposition, and the reaction process tends to transform into a lithium free/low lithium spinel/rock salt intermediate phase, which further transforms into a layered structure with increasing temperature. This layered phase transition pathway of spinel requires a higher energy barrier and is relatively more difficult to fully transform into a layered structure, resulting in an impact on the microstructure and electrochemical performance of the final synthesized material. The above results clarify the reaction mechanism from precursor to finished product, which can better guide the rational selection and design of raw materials and lithium sources in the synthesis process of LMLO.

ASSOCIATED CONTENT

Supporting Information

The Supporting Information is available free of charge at https://pubs.acs.org/doi/10.1021/acsomega.3c09567.

SEM images and EDS mapping; XRD patterns; TG-MS curves; Raman spectra; rate capabilities; ICP-OES analysis; and XRD reference of different phases (PDF)

AUTHOR INFORMATION

Corresponding Author

Zhen-guo Wu − *School of Chemical Engineering, Sichuan University, Chengdu 610065, China;* Present Address: School of Chemical Engineering, Sichuan University, Chengdu, 610065, PR China;; orcid.org/0000-0002-8153-2169; Email: zhenguowu@scu.edu.cn

Authors

Chen Wu − *Natural Gas Research Institute, PetroChina Southwest Oil and Gas Field Company, Chengdu 610213, PR China;* Present Address: Natural Gas Research Institute, PetroChina Southwest Oil and Gas Field Company, Chengdu 610213, PR China;

Jiuqing Ban − *Natural Gas Research Institute, PetroChina Southwest Oil and Gas Field Company, Chengdu 610213, PR China;* Present Address: Natural Gas Research Institute, PetroChina Southwest Oil and Gas Field Company, Chengdu 610213, PR China;; orcid.org/0000-0003-4586-8121

Ting Chen − *School of Chemical Engineering, Sichuan University, Chengdu 610065, China; Institute for Advanced*

https://doi.org/10.1021/acsomega.3c09567
ACS Omega 2024, 9, 15191−15201

Study, Chengdu University, Chengdu 610106, PR China; Present Address: School of Chemical Engineering, Sichuan University, Chengdu, 610065, PR China;; Present Address: Institute for Advanced Study, Chengdu University, Chengdu 610106, PR China;

Jie Wang − *Shunan Gas Mine of PetroChina Southwest Oil and Gas Field Company, Luzhou 646000, PR China;* Present Address: Shunan Gas Mine of PetroChina Southwest Oil and Gas Field Company, Luzhou 646000, PR China

Yangdong He − *Natural Gas Research Institute, PetroChina Southwest Oil and Gas Field Company, Chengdu 610213, PR China;* Present Address: Natural Gas Research Institute, PetroChina Southwest Oil and Gas Field Company, Chengdu 610213, PR China;

Complete contact information is available at: https://pubs.acs.org/10.1021/acsomega.3c09567

Notes

The authors declare no competing financial interest.

■ ACKNOWLEDGMENTS

This work was supported by the Research topics for scientific research and technological development projects of China National Petroleum Corporation (grant no. 2021DJ5302) and Technology Plan Project of PetroChina Southwest Oil and Gas Field Company (grant no. 20230312-05).

■ REFERENCES

(1) Yang, J.; Liang, X.; Ryu, H.-H.; Yoon, C. S.; Sun, Y.-K. Ni-rich layered cathodes for lithium-ion batteries: From challenges to the future. *Energy Storage Mater.* **2023**, *63*, 102969.

(2) Chu, B.; You, L.; Li, G.; Huang, T.; Yu, A. Revealing the Role of W-Doping in Enhancing the Electrochemical Performance of the LiNi0.6Co0.2Mn0.2O2 Cathode at 4.5 V. *ACS Appl. Mater. Interfaces* **2021**, *13* (6), 7308−7316.

(3) Zhang, S. S. Problems and their origins of Ni-rich layered oxide cathode materials. *Energy Storage Mater.* **2020**, *24*, 247−254.

(4) Li, W.; Erickson, E. M.; Manthiram, A. High-nickel layered oxide cathodes for lithium-based automotive batteries. *Nat. Energy* **2020**, *5* (1), 26−34.

(5) Han, Z.; Zhao, S.; Xiao, J.; Zhong, X.; Sheng, J.; Lv, W.; Zhang, Q.; Zhou, G.; Cheng, H. M. Engineering d-p Orbital Hybridization in Single-Atom Metal-Embedded Three-Dimensional Electrodes for Li-S Batteries. *Adv. Mater.* **2021**, *33* (44), 2105947.

(6) Zhao, J.; Liang, Y.; Zhang, X.; Zhang, Z.; Wang, E.; He, S.; Wang, B.; Han, Z.; Lu, J.; Amine, K.; et al. In Situ Construction of Uniform and Robust Cathode-Electrolyte Interphase for Li-Rich Layered Oxides. *Adv. Funct. Mater.* **2020**, *31*(8)..

(7) Wang, E.; Zhao, Y.; Xiao, D.; Zhang, X.; Wu, T.; Wang, B.; Zubair, M.; Li, Y.; Sun, X.; Yu, H. Composite Nanostructure Construction on the Grain Surface of Li-Rich Layered Oxides. *Adv. Mater.* **2020**, *32* (49), 1906070.

(8) Hafiz, H.; Suzuki, K.; Barbiellini, B.; Tsuji, N.; Yabuuchi, N.; Yamamoto, K.; Orikasa, Y.; Uchimoto, Y.; Sakurai, Y.; Sakurai, H.; Bansil, A.; Viswanathan, V. Tomographic reconstruction of oxygen orbitals in lithium-rich battery materials. *Nature* **2021**, *594* (7862), 213−216.

(9) Lee, J.; Dupre, N.; Jeong, M.; Kang, S.; Avdeev, M.; Gong, Y.; Gu, L.; Yoon, W. S.; Kang, B. Fully Exploited Oxygen Redox Reaction by the Inter-Diffused Cations in Co-Free Li-Rich Materials for High Performance Li-Ion Batteries. *Adv. Sci.* **2020**, *7* (17), 2001658.

(10) Zeng, W.; Liu, F.; Yang, J.; Zhang, B.; Cao, F.; Tian, W.; Wang, J.; Yu, R.; Xia, F.; Peng, H.; et al. Single-crystal Li-rich layered cathodes with suppressed voltage decay by double-layer interface engineering. *Energy Storage Mater.* **2023**, *54*, 651−660.

(11) Yang, W.; Li, H.; Wang, D.; Xu, C.; Xiang, W.; Song, Y.; He, F.; Zhang, J.; Zheng, B.; Zhong, B.; et al. Ta induced fine tuning of microstructure and interface enabling Ni-rich cathode with unexpected cyclability in pouch-type full cell. *Nano Energy* **2022**, *104*, 107880.

(12) Wu, C.; Li, R.; Chen, T.; Hu, T.; Wang, D.; Qiu, L.; Zhong, B.; Wu, Z.; Guo, X. Understanding of the Irreversible Phase Transition and Zr-Doped Modification Strategy for a Nickel-Rich Cathode under a High Voltage. *ACS Sustainable Chem. Eng.* **2022**, *10* (11), 3651−3660.

(13) Xu, C.; Xiang, W.; Wu, Z.; Xu, Y.; Li, Y.; Wang, Y.; Xiao, Y.; Guo, X.; Zhong, B. Highly Stabilized Ni-Rich Cathode Material with Mo Induced Epitaxially Grown Nanostructured Hybrid Surface for High-Performance Lithium-Ion Batteries. *ACS Appl. Mater. Interfaces* **2019**, *11* (18), 16629−16638.

(14) Hua, W.; Wu, Z.; Chen, M.; Knapp, M.; Guo, X.; Indris, S.; Binder, J. R.; Bramnik, N. N.; Zhong, B.; Guo, H.; et al. Shape-controlled synthesis of hierarchically layered lithium transition-metal oxide cathode materials by shear exfoliation in continuous stirred-tank reactors. *J. Mater. Chem. A* **2017**, *5* (48), 25391−25400.

(15) Chen, L.; Su, Y.; Chen, S.; Li, N.; Bao, L.; Li, W.; Wang, Z.; Wang, M.; Wu, F. Hierarchical Li1.2 Ni0.2 Mn0.6 O2 nanoplates with exposed {010} planes as high-performance cathode material for lithium-ion batteries. *Adv. Mater.* **2014**, *26* (39), 6756−6760.

(16) Rahman, M. T.; Mireles, K.; Gomez Chavez, J. J.; Wo, P. C.; Marcial, J.; Kessler, M. R.; McCloy, J.; Ramana, C. V.; Panat, R. High Temperature Physical and Chemical Stability and Oxidation Reaction Kinetics of Ni-Cr Nanoparticles. *J. Phys. Chem. C* **2017**, *121* (7), 4018−4028.

(17) Hua, W.; Yang, X.; Wang, S.; Li, H.; Senyshyn, A.; Tayal, A.; Baran, V.; Chen, Z.; Avdeev, M.; Knapp, M.; et al. Dynamic inconsistency between electrochemical reaction and phase transition in Na-deficient layered cathode materials. *Energy Storage Mater.* **2023**, *61*, No. 102906.

(18) Lin, C.; Li, J.; Yin, Z. W.; Huang, W.; Zhao, Q.; Weng, Q.; Liu, Q.; Sun, J.; Chen, G.; Pan, F. Structural Understanding for High-Voltage Stabilization of Lithium Cobalt Oxide. *Adv. Mater.* **2023**, *36*, 2307404.

(19) Wang, D.; Kou, R.; Ren, Y.; Sun, C. J.; Zhao, H.; Zhang, M. J.; Li, Y.; Huq, A.; Ko, J. Y. P.; Pan, F.; et al. Synthetic Control of Kinetic Reaction Pathway and Cationic Ordering in High-Ni Layered Oxide Cathodes. *Adv. Mater.* **2017**, *29*(39)..

(20) Qiu, L.; Song, Y.; Zhang, M.; Liu, Y.; Yang, Z.; Wu, Z.; Zhang, H.; Xiang, W.; Liu, Y.; Wang, G.; et al. Structural Reconstruction Driven by Oxygen Vacancies in Layered Ni-Rich Cathodes. *Adv. Energy Mater.* **2022**, *12*(19)..

(21) Yu, H.; So, Y. G.; Ren, Y.; Wu, T.; Guo, G.; Xiao, R.; Lu, J.; Li, H.; Yang, Y.; Zhou, H.; et al. Temperature-Sensitive Structure Evolution of Lithium-Manganese-Rich Layered Oxides for Lithium-Ion Batteries. *J. Am. Chem. Soc.* **2018**, *140* (45), 15279−15289.

(22) Bianchini, M.; Wang, J.; Clement, R. J.; Ouyang, B.; Xiao, P.; Kitchaev, D.; Shi, T.; Zhang, Y.; Wang, Y.; Kim, H.; et al. The interplay between thermodynamics and kinetics in the solid-state synthesis of layered oxides. *Nat. Mater.* **2020**, *19* (10), 1088−1095.

(23) Bai, J.; Sun, W.; Zhao, J.; Wang, D.; Xiao, P.; Ko, J. Y. P.; Huq, A.; Ceder, G.; Wang, F. Kinetic Pathways Templated by Low-Temperature Intermediates during Solid-State Synthesis of Layered Oxides. *Chem. Mater.* **2020**, *32* (23), 9906−9913.

(24) Wang, S.; Hua, W.; Missyul, A.; Darma, M. S. D.; Tayal, A.; Indris, S.; Ehrenberg, H.; Liu, L.; Knapp, M. Kinetic Control of Long-Range Cationic Ordering in the Synthesis of Layered Ni-Rich Oxides. *Adv. Funct. Mater.* **2021**, *31*..

(25) Shi, J. L.; Xiao, D. D.; Ge, M.; Yu, X.; Chu, Y.; Huang, X.; Zhang, X. D.; Yin, Y. X.; Yang, X. Q.; Guo, Y. G.; et al. High-Capacity Cathode Material with High Voltage for Li-Ion Batteries. *Adv. Mater.* **2018**, *30*(9)..

(26) Peng, H.; Zhuo, H.; Xia, F.; Zeng, W.; Sun, C.; Wu, J. Effects of Bending on Nucleation and Injection of Oxygen Vacancies into the Bulk Lattice of Li-Rich Layered Cathodes. *Adv. Funct. Mater.* **2023**, *33*, 2306804.

(27) Hua, W.; Wang, S.; Knapp, M.; Leake, S. J.; Senyshyn, A.; Richter, C.; Yavuz, M.; Binder, J. R.; Grey, C. P.; Ehrenberg, H.; et al. Structural

insights into the formation and voltage degradation of lithium- and manganese-rich layered oxides. *Nat. Commun.* **2019**, *10* (1), 5365.
(28) Wu, C.; Qiu, L.; Wang, D.-q.; Chen, T.; Li, J.; Wu, Z.-g.; Song, Y.; Guo, X.-d. New Insight into High-Rate Performance Lithium-Rich Cathode Synthesis through Controlling the Reaction Pathways by Low-Temperature Intermediates. *Ind. Eng. Chem. Res.* **2022**, *61* (1), 453−463.
(29) Huang, W.; Lin, C.; Zhang, M.; Li, S.; Chen, Z.; Zhao, W.; Zhu, C.; Zhao, Q.; Chen, H.; Pan, F. Revealing Roles of Co and Ni in Mn-Rich Layered Cathodes. *Adv. Energy Mater.* **2021**, *11*(41)..
(30) Sheng, H.; Meng, X. H.; Xiao, D. D.; Fan, M.; Chen, W. P.; Wan, J.; Tang, J.; Zou, Y. G.; Wang, F.; Wen, R.; et al. An Air-Stable High-Nickel Cathode with Reinforced Electrochemical Performance Enabled by Convertible Amorphous Li(2) CO(3) Modification. *Adv. Mater.* **2022**, *34* (12), No. e2108947.
(31) Song, S. H.; Hong, S.; Cho, M.; Yoo, J.-G.; Min Jin, H.; Lee, S.-H.; Avdeev, M.; Ikeda, K.; Kim, J.; Nam, S. C.; et al. Rational design of Li off-stoichiometric Ni-rich layered cathode materials for Li-ion batteries. *Chem. Eng. J.* **2022**, *448*, No. 137685.
(32) Park, G.-T.; Ryu, H.-H.; Noh, T.-C.; Kang, G.-C.; Sun, Y.-K. Microstructure-optimized concentration-gradient NCM cathode for long-life Li-ion batteries. *Mater. Today* **2022**, *52*, 9−18.
(33) Pokle, A.; Weber, D.; Bianchini, M.; Janek, J.; Volz, K. Probing the Ni(OH)(2) Precursor for LiNiO(2) at the Atomic Scale: Insights into the Origin of Structural Defect in a Layered Cathode Active Material. *Small* **2023**, *19* (4), 2205508.
(34) Zhang, M. J.; Teng, G.; Chen-Wiegart, Y. c. K.; Duan, Y.; Ko, J. Y. P.; Zheng, J.; Thieme, J.; Dooryhee, E.; Chen, Z.; Bai, J.; et al. Cationic Ordering Coupled to Reconstruction of Basic Building Units during Synthesis of High-Ni Layered Oxides. *J. Am. Chem. Soc.* **2018**, *140* (39), 12484−12492.
(35) Liu, W.; Oh, P.; Liu, X.; Myeong, S.; Cho, W.; Cho, J. Countering Voltage Decay and Capacity Fading of Lithium-Rich Cathode Material at 60 °C by Hybrid Surface Protection Layers. *Adv. Energy Mater.* **2015**, *5*(13)..
(36) Lai, J.; Zhang, J.; Li, Z.; Xiao, Y.; Hua, W.; Wu, Z.; Chen, Y.; Zhong, Y.; Xiang, W.; Guo, X. Structural elucidation of the degradation mechanism of nickel-rich layered cathodes during high-voltage cycling. *Chem. Commun.* **2020**, *56* (36), 4886−4889.
(37) Zheng, J.; Liu, T.; Hu, Z.; Wei, Y.; Song, X.; Ren, Y.; Wang, W.; Rao, M.; Lin, Y.; Chen, Z.; et al. Tuning of Thermal Stability in Layered $Li(Ni_xMn_yCo_z)O_2$. *J. Am. Chem. Soc.* **2016**, *138* (40), 13326−13334.
(38) Wang, F.; Bai, J. Synthesis and Processing by Design of High-Nickel Cathode Materials. *Batteries Supercaps* **2021**, *5*(1)..
(39) Hua, W.; Chen, M.; Schwarz, B.; Knapp, M.; Bruns, M.; Barthel, J.; Yang, X.; Sigel, F.; Azmi, R.; Senyshyn, A.; et al. Lithium/Oxygen Incorporation and Microstructural Evolution during Synthesis of Li-Rich Layered Li[Li0.2Ni0.2Mn0.6]O2 Oxides. *Adv. Energy Mater.* **2019**, *9*(8)..
(40) Hua, W.; Wang, K.; Knapp, M.; Schwarz, B.; Wang, S.; Liu, H.; Lai, J.; Müller, M.; Schökel, A.; Missyul, A.; et al. Chemical and Structural Evolution during the Synthesis of Layered Li(Ni,Co,Mn)O2 Oxides. *Chem. Mater.* **2020**, *32* (12), 4984−4997.
(41) Sun, G.; Yu, F.-D.; Que, L.-F.; Deng, L.; Wang, M.-J.; Jiang, Y.-S.; Shao, G.; Wang, Z.-B. Local electronic structure modulation enhances operating voltage in Li-rich cathodes. *Nano Energy* **2019**, *66*, No. 104102.

https://doi.org/10.1021/acsomega.3c09567
ACS Omega 2024, 9, 15191−15201